Spherical deconvolution with tissue-specific response functions and multi-shell diffusion MRI to estimate multiple fiber orientation distributions (mFODs)

Alberto De Luca[1], Fenghua Guo[1], Martijn Froeling[2], Alexander Leemans[1]
[1]Image Sciences Institute, UMC Utrecht, Utrecht, the Netherlands
[2]Department of Radiology, UMC Utrecht, Utrecht, the Netherlands

Corresponding author: Alberto De Luca
Heidelberglaan 100, 3584CX
Utrecht, the Netherlands

Early draft

Word count: 5728

Key words: diffusion MRI, FOD, white matter, grey matter, fiber tractography

Abstract

In diffusion MRI, spherical deconvolution approaches can resolve local white matter (WM) fiber orientation distributions (FOD) to produce state-of-the-art fiber tractography reconstructions. In contrast, spherical deconvolution typically produces suboptimal results in grey matter (GM). The advent of multi-shell diffusion MRI data has seen a growing interest toward GM, but its modelling remains confined to that of an isotropic diffusing process. However, evidence from both histology and high-resolution diffusion MRI studies suggests a marked anisotropic character of the diffusion process in GM, which might be exploited by appropriate modelling to improve the description of the cortical organization. Indeed, improving the performance of spherical deconvolution in GM might allow to track WM bundles to their start/endpoint in the cortex, a crucial step to improve the accuracy of fiber tractography reconstructions. In this study, we investigated whether performing spherical deconvolution with tissue specific models of both WM and GM improves the FOD characterization in GM while also retaining state-of-the-art performances in WM. To this end, we devised a framework able to simultaneously accommodate multiple tissue response functions, to estimate multiple, tissue-specific, fiber orientation distributions (mFOD.) As proof of principle, we used the diffusion kurtosis imaging model to represent the WM signal, and the neurite orientation dispersion and density imaging (NODDI) model to represent the GM signal. The feasibility of mFOD is shown with numerical simulations, then the performances of the method were compared to gold-standard multi-shell constrained spherical deconvolution (MSCSD) with data of a subject from the Human Connectome Project (HCP). Results of simulations show mFOD can accurately estimate mixture of two FODs given sufficient SNR (≥ 50 at $b = 0 s/mm^2$) is achieved. With HCP data, mFOD provided improved FOD estimation in GM as compared to MSCSD, whereas the performances of the two methods were comparable in WM. When performing fiber tractography, tracts with mFOD entered the cortex with more spatial contiguity and for a longer distance as compared to MSCSD. In conclusion, mFOD allows to perform spherical deconvolution of multiple anisotropic response functions, improving the performances of spherical deconvolution in grey matter.

Introduction

Diffusion Magnetic Resonance Imaging (dMRI) is a non-invasive technique sensitive to the microscopic motion (diffusion process) of water molecules[1]. In biologic tissues, the diffusion process is influenced by the presence of biologic membranes and macromolecules[2], which can hinder or restrict the molecular random walk in both isotropic and anisotropic manners. In the '90s, Basser et al.[3] characterized the anisotropy of hindered diffusion processes, proposing the diffusion tensor imaging (DTI) framework. Later, it was shown that when the diffusion process exhibits sufficient anisotropy, its principal direction can be computed[3] and eventually tracked[4]. This approach can be applied, for instance, to reconstruct the configuration of brain white matter (WM) with fiber tractography[5,6].

DTI-based fiber tractography is acquisition and computation efficient but suffers of a number of limitations. Firstly, the technique fails when multiple diffusion processes – i.e. multiple pathways – coexist in the same spatial location[7], which is the case in over 90% of the human WM[8] and is not likely to be solved by technological improvements as higher imaging resolutions[9]. Secondly, DTI-based fiber tractography only applies to data acquired within the Gaussian diffusion regime, and thus cannot take advantage of the higher angular resolution provided by strong diffusion weightings[10]. For this reason, DTI is not likely not the method of choice in a heterogeneous structure as grey matter (GM), which is characterized by low fractional anisotropy and hence high uncertainty of the principal diffusion direction.

Spherical deconvolution approaches[11,12] effectively solve the first two limitations, and are the current gold standard to reconstruct fiber orientation distribution (FOD) and to perform fiber tractography in WM. However, their application to the study of GM remains limited, as FODs derived in the cortex are noisy and exhibit spurious peaks, a challenge when performing fiber tractography. Importantly, limitations in fiber tractography propagate to other analysis techniques making use of fiber reconstructions as, among others, structural connectivity approaches[13]. Indeed, fiber tracking is often seeded (or terminated) at the grey/white matter interface, but the inability to properly follow WM bundles in the cortex generates uncertainty onto the endpoints of the bundles. This has been partially addressed with geometric heuristics[14], but these oversimplify the way axons traverse the cortex[15].

The advent of specialized techniques for diffusion imaging, such as ultra-strong gradients[16] and simultaneous multi-slice[17], are rapidly increasing the imaging quality and resolution achievable in dMRI, allowing to appreciate new details of the human cortex, as reviewed by Assaf[18]. In ex-vivo studies[15,19,20], it has been consistently shown that the diffusion process observed in the cortex has a large anisotropic component perpendicular to the cortical folding, but also that tangential directions can be observed, for instance, in the central sulcus[21]. Such high-quality data acquisitions may soon be available for in-vivo applications, offering unprecedented research possibilities[22] in fiber tractography of GM, but a dedicated framework has not yet been investigated.

Recently, multi-tissue spherical deconvolution approaches[23] have been suggested to further increase the accuracy of FOD reconstructions in WM by accounting for partial volume effects, e.g. in spatial locations where WM overlaps with GM or cerebrospinal fluid (CSF). Although GM and CSF are merely considered nuisance factors[24], such framework highlights the feasibility of explicitly accounting for multiple tissues in spherical deconvolution approaches. By separating multiple partial volume effects, multi-tissue approaches have shown improved FOD reconstructions in adults[23], neonates[25] and in patients with Parkinson's disease[26]. In current state-of-the-art multi-shell spherical deconvolution, only WM is assumed

to be isotropic, while GM is regarded as characterized by isotropic diffusion. To estimate the WM FOD, a WM fiber model – or response function – is estimated from voxels with single fiber population, which are typically located in large bundles[27] such as, for example, the corpus callosum or the corticospinal tract. The response function is then assumed to be valid throughout the brain. While the validity of this representation has been questioned even in WM itself[28], it is highly unlikely that it can adequately represent the anisotropic signature of axons and dendrites in the cortex.

In this study, we investigate whether the spherical deconvolution problem can be revisited to take into account the different signal characteristics of WM and GM, by explicitly modelling both signal mixtures simultaneously. This novel formulation allows to reconstruct multiple FODs (mFODs) and is ultimately aimed at improving the FOD estimation and fiber tractography of GM while retaining state-of-the-art performances in WM. In mFOD, we disregard the existence of a single response function for the brain, and investigate whether it is feasible to i) simultaneously estimate multiple anisotropic FODs corresponding to tissue-specific response functions, and whether this improves ii) the fiber orientation characterization in GM, and iii) fiber tractography in GM as compared to existing spherical deconvolution methods.

Methods

The following paragraphs present the mFOD framework and explain the qualitative and quantitative analysis that we performed using both simulations and in-vivo data.

Theory: multi-shell Richardson Lucy (mRL)

In a previous work[29], we introduced a multi-shell spherical deconvolution framework based on the Richardson-Lucy (mRL) framework to account for multiple tissue types, such as WM, GM and cerebrospinal-fluid (CSF), as shown in Eq. 1.

$$\frac{S}{S_0} = f_{WM}\begin{bmatrix} \mathrm{H}^1_{\mathrm{WM,1}} & \cdots & \mathrm{H}^1_{\mathrm{WM,k}} \\ \vdots & \ddots & \vdots \\ \mathrm{H}^n_{\mathrm{WM,1}} & \cdots & \mathrm{H}^n_{\mathrm{WM,k}} \end{bmatrix} \otimes \mathrm{FOD}_{\mathrm{WM}} + f_{GM}\begin{bmatrix} \mathrm{H}^1_{\mathrm{GM}} \\ \vdots \\ \mathrm{H}^1_{\mathrm{GM}} \end{bmatrix} + f_{CSF}\begin{bmatrix} \mathrm{H}^1_{\mathrm{CSF}} \\ \vdots \\ \mathrm{H}^1_{\mathrm{CSF}} \end{bmatrix} \qquad [1]$$

In the equation above, S is the signal collected at n diffusion weightings, S_0 is the non-weighted signal, H represents the signal model associated to WM, GM and CSF, respectively, f is the associated signal fraction, and FOD is the fiber orientation distribution associated to WM. The columns of the deconvolution matrix shown in Eq. 1 represent the possible solution of the spherical deconvolution on the unit sphere, resulting in a total number of k+2 columns, as GM and CSF are both considered isotropic.

Theory: mFOD

In the mFOD framework, we redesigned the deconvolution matrix to allow for an arbitrary number of independent anisotropic deconvolution models. Considering to solve the spherical deconvolution problem once more for WM, GM and CSF, but now accounting for anisotropic diffusion in both WM and GM, we can write:

$$\frac{S}{S_0} = \begin{bmatrix} \mathrm{H}^1_{\mathrm{WM,1}} & \cdots & \mathrm{H}^1_{\mathrm{WM,k}} & \mathrm{H}^1_{\mathrm{GM,1}} & \cdots & \mathrm{H}^1_{\mathrm{GM,k}} \\ \vdots & \ddots & \vdots & \vdots & \ddots & \vdots \\ \mathrm{H}^n_{\mathrm{WM,1}} & \cdots & \mathrm{H}^n_{\mathrm{WM,k}} & \mathrm{H}^n_{\mathrm{WM,1}} & \cdots & \mathrm{H}^n_{\mathrm{GM,k}} \end{bmatrix} \otimes \begin{bmatrix} \mathrm{FOD}_{\mathrm{WM}} \\ \mathrm{FOD}_{\mathrm{GM}} \end{bmatrix} \begin{bmatrix} f_{\mathrm{WM}} \\ f_{\mathrm{GM}} \end{bmatrix} + f_{CSF}\begin{bmatrix} \mathrm{H}^1_{\mathrm{CSF}} \\ \vdots \\ \mathrm{H}^1_{\mathrm{CSF}} \end{bmatrix} \qquad [2]$$

Eq. [2] can be solved using the iterative least-squares minimizer previously introduced for mDRL but replacing the Richardson-Lucy deconvolution scheme with a regularized non-negative least-squares solver[30], producing 2 independent FODs.

Signal models

To underline the model independence of the mFOD framework, the H-matrices of WM, GM and CSF, shown in Eq. 2, were generated with three different models. H_{CSF} was generated using the ADC model and the typical diffusion coefficient of free water at 37 degrees ($3.0 \times 10^{-3} mm^2/s$). The columns of H_{WM} and H_{GM} were generated using instances of the DKI model[31] with isotropic kurtosis[32], and of the NODDI model[33], respectively, both in simulations and with in-vivo data. The parameters of the models were determined as explained in the following paragraphs. The DKI model was chosen as it can represent the anisotropy of the WM signal while also taking into account non-Gaussian diffusion effects. The NODDI model has been shown to characterize the GM microstructure better than tensor models[34], and allows to take into account the larger presence of cell bodies in GM as compared to WM.

Simulations

The feasibility of simultaneously computing multiple anisotropic FOD corresponding to different models was evaluated numerically. H_{WM} was generated with the DKI model by considering eigenvalues (1.7, 0.3, 0.3) x $10^{-3} mm^2/s$, and isotropic kurtosis equal to 0.6. H_{GM} was generated with the NODDI model by simulating values of intra to extra-cellular ratio 0.4, parallel diffusivity $1.7 \times 10^{-3} mm^2/s$, the concentration parameter of the Watson distribution was set to 1.0, and no partial volume of free-water was considered as mFOD explicitly accounts for it. The parameters used for generating H_{WM} and H_{GM} matched the average values observed with in-vivo data.

Two set of simulations were generated. Simulation I aimed to evaluate the robustness to noise of mFOD, whereas simulation II characterized the ability of mFOD at separating partial volume effects for a given SNR level.

Simulation I

Three configurations were generated by considering partial volume effects between i) WM and CSF, ii) GM and CSF, iii) WM and GM. The simulated partial volume ratio was 0.8/0.2, with an angle of approximately 90 degrees between the main direction of WM and the main direction of GM. The effect of noise was simulated by adding 1000 Rician realizations in correspondence of SNR levels 10, 20, 30, 40, 50, 60, 70, 150. For each SNR level, we evaluated the error between the estimated and the simulated signal fractions, as well as the error between the simulated and the estimated main diffusion direction.

Simulation II

Three partial volume configurations were generated in analogy with simulation I but increasing the ratio between the two simulated tissues from 0 to 1 with step 0.1. Rician noise was added by considering 1000 realizations at SNR 50. The error between the simulated and the estimated signal fractions was determined.

In-vivo data processing

A subject from the Human Connectome Project (HCP) was included in this study. The dataset included a T1-weighted image acquired at a resolution of 0.7mm isotropic, and a dMRI dataset acquired at 1.25mm isotropic. The diffusion dataset consisted of 18 b = 0 s/mm^2 volumes in addition to 270 volumes acquired

by sampling diffusion weightings b = 1000, 2000, 3000 s/mm^2 along 90 directions each. The T1-weighted data was rigidly registered to the pre-processed dMRI data, then the tissue type segmentations of WM, GM and CSF were derived with FSL FAST.

Determining the H-matrix

The dMRI data was fit with both the MSCSD and the mFOD approaches using custom implementations in MATLAB R2018b (The Mathworks Inc.) and functions from the ExploreDTI toolbox[35]. MSCSD was initialized as previously suggested by using the tissue maps derived from the T1-weighted image. For the generation of the H-matrices used for mFOD, a whole brain DKI and NODDI fit were performed. For the WM H-matrix, the eigenvalues of the diffusion tensor and the isotropic kurtosis were averaged within a white matter mask defined by fractional anisotropy values above 0.7. This resulted in eigenvalues [1.3, 0.5, 0.5]x10^{-3}mm^2/s and isotropic kurtosis value 0.64. For the GM H-matrix, the NODDI metrics were averaged within the GM segmentation obtained with the T1-weighted image, which resulted in intra to extra-cellular ratio 0.4, parallel diffusivity 1.7x10^{-3}mm^2/s and Watson's concentration parameter equal to 1.

FODs and signal fractions

The MSCSD fit produced signal fractional maps associated to WM, GM and CSF, and one FOD describing WM orientations. The fit of mFOD resulted in the same number of fractional maps but two FODs, mFOD$_1$ describing WM geometry, and mFOD$_2$ describing GM geometry, respectively.

Comparison of signal fractions

The signal fraction maps computed with MSCSD and mFOD were qualitatively compared to those obtained from the T1-weighted volume. Further, the FODs computed with MSCSD and mFOD were compared in selected cortical areas, to qualitatively determine whether mFOD$_2$ provided additional information in GM as compared to mFOD$_1$ and MSCSD.

Quantitative analysis of FODs

The FODs computed with mFOD can be either analyzed separately, or merged to combine accurate geometrical information in both WM and GM. In name of clarity and purely as proof of concept, we combined the two FODs by considering their normalized sum weighted by the respective signal fractions (mFOD-WS).

One of the difficulties when validating in-vivo dMRI techniques is the lack of ground truth. MSCSD can be regarded as the gold standard in WM, but not in GM. In a first analysis, we aimed to establish to which extent the principal diffusion directions of mFOD-WS agree with those of MSCSD in both WM and GM. Up to three peaks were voxel-wise identified for both FODs, then sorted per descending amplitude values. Subsequently, the angle between MSCSD and mFOD-WS was determined as the minimum dyadic angle between any pair of peaks.

If discrepancies are observed in GM, it remains impossible to ultimately judge which method is the most accurate, but comparisons with a third method could provide insights if not conclusions. Anatomical knowledge as well as previous MRI studies[22] suggest that the dominant diffusion directions in GM should be perpendicular to the cortical folding, with exceptions such as the primary visual cortex[15]. We therefore derived the normal vectors to the cortical folding by using an in-house method based on the structural tensor[36] and computed the minimum dyadic angle between the absolute value of the cortex normal vectors and the absolute value of the vectors dictated by the first three diffusion directions of MSCSD and mFOD-WS.

Fiber tractography

Tracking parameters

We investigated the results obtained by performing fiber tractography with MSCSD, $mFOD_1$, $mFOD_2$ and mFOD-WS both qualitatively and quantitatively, with intentional focus on GM areas. Deterministic fiber tractography was performed in ExploreDTI by using identical parameters for all methods: FOD threshold 0.1 (default), minimum/maximum fiber length equal to 20/500mm, angle threshold 45 degrees, step-size 0.6mm.

Quantitative analysis

Firstly, FODs computed with MSCSD and mFOD-WS were seeded in a frontal region and color encoded with a custom colormap assigning red, yellow and blue to tracts traversing WM, GM and CSF, respectively. Subsequently, whole brain tractography of all FODs was performed by seeding all voxels with an FOD value above the default threshold. The tracts were color encoded both with the conventional RGB color scheme[37] and the above-mentioned tissue-type color scheme, to convey both directional information and specificity of the FODs to different tissue types.

Tracts in a 3.75mm wide sagittal slab were color encoded by normalized distance between the GM/WM interface and the WM/CSF interface, obtained from the T1-weighted segmentation, as well as by tissue type, to appreciate differences in GM tracking distance / density between the compared methods.

Quantitatively, we evaluated how many tracts were generated with MSCSD and mFOD-WS, which is informative given the seed-points were kept constant and a deterministic tracking algorithm was used. Additionally, we counted the fraction of plausible tracts, i.e. tracts having at least one end-point in grey matter, as well as the spatial coverage of GM when considering only start/end points of tracts.

Results

Simulations

Figure 1 shows the signal fractions estimated with mFOD in simulation I, where different mixtures of WM, GM and CSF were simulated for multiple SNR Levels. At SNR level equal or greater than 20, mFOD disentangles mixtures of WM and CSF with signal fraction errors below 2% and angular errors below 3 degrees. The separation of GM from both WM and CSF is more challenging and requires higher SNR to achieve an error below 10%. In both cases, the signal fraction errors at SNR 50 are about 9%, 11% and 2%, for WM, GM and CSF, respectively. At the same SNR level, the angular error on the GM FOD is 8 degrees for the GM and CSF mixture. With regards to the GM and WM mixture, the angular errors of the WM and GM FODs are 4 degrees and 10 degrees, respectively.

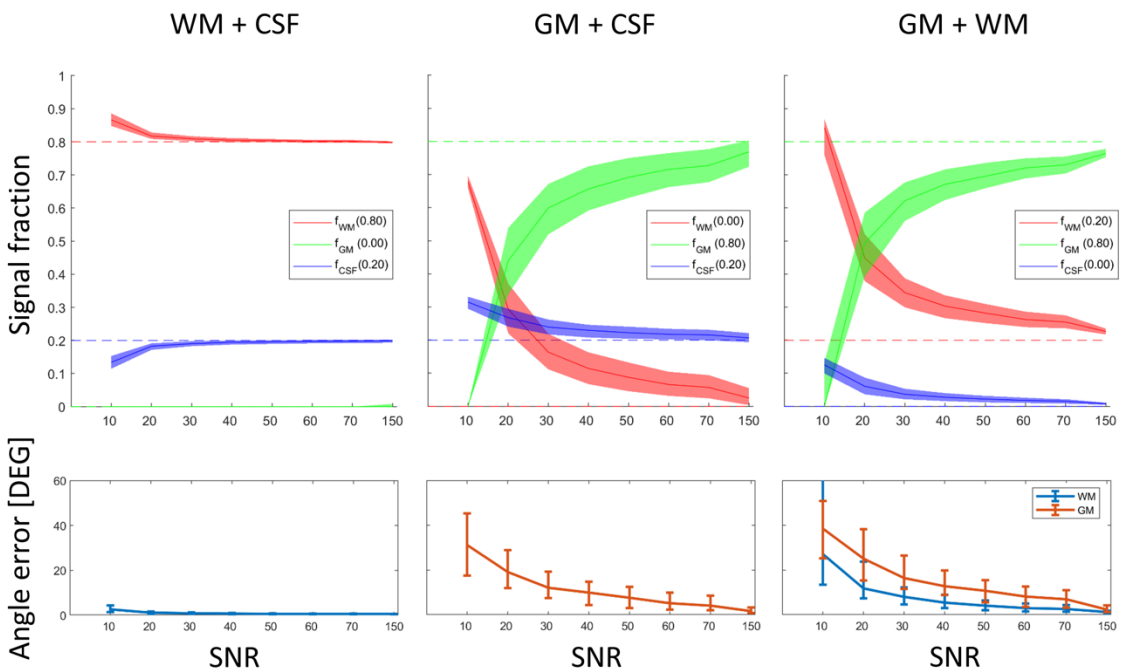

Figure 1: Results of simulation I. The first row shows the 25th – 75th percentile (shaded area) and the median (solid line) of the signal fractions estimated with mFOD for different SNR levels and partial volume mixtures (each column). The second row shows the angular error of the main direction of the WM and GM FODs as compared to the ground truth value. The solid line represents the median value, whereas the error bars the 25th and 75th percentile. The simulations were performed using anisotropic response functions for WM and GM, and an isotropic response function for CSF. To properly detect the main peak orientation associated to GM, a high SNR (≥50) is required.

Figure 2 shows the signal fractions estimated in simulation II when linearly varying the simulated WM, GM and CSF fractions at SNR 50. For all the three cases, the estimated average signal fractions show excellent agreement with the simulated values. The maximum errors observed for the three classes are 13%, 20% and 4%, respectively. The Pearson correlation coefficient between the simulated and estimated signal fractions have values between 0.99 and 1.

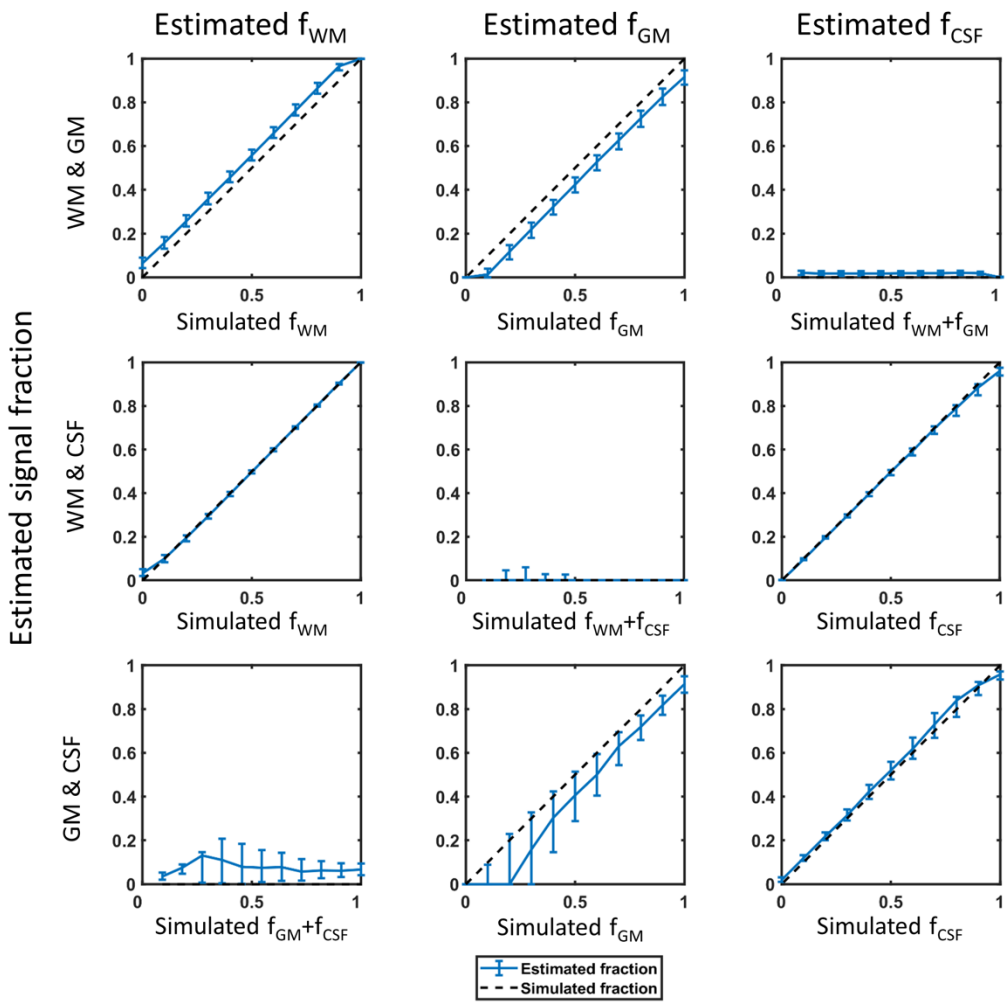

Figure 2: The median value (solid line) and the 25th – 75th percentile (error bars) of the signal fractions estimated with mFOD for the simulated anisotropic WM and GM response functions (columns 1-2) and the isotropic CSF response function (column 3). Different mixtures of the three tissue types were realized with increasing partial volume and 1000 realizations of Rician noise at SNR 50. The largest errors were observed in occurrence of GM and CSF mixtures for low GM signal fractions.

HCP data

Signal fractions

The WM, GM and CSF signal fractions estimated with MSCSD and mFOD, as well as those derived from the segmentation of the T1-weighted image are shown for an example axial slice in Fig. 3. The maps estimated with mFOD exhibit excellent agreement with both MSCSD and the T1-derived segmentation, despite the numerical ill-conditioning of the mFOD problem. The WM fractional maps estimated with both MSCSD and mFOD have non-zero values also in some GM areas, in contrast to the T1-derived segmentation.

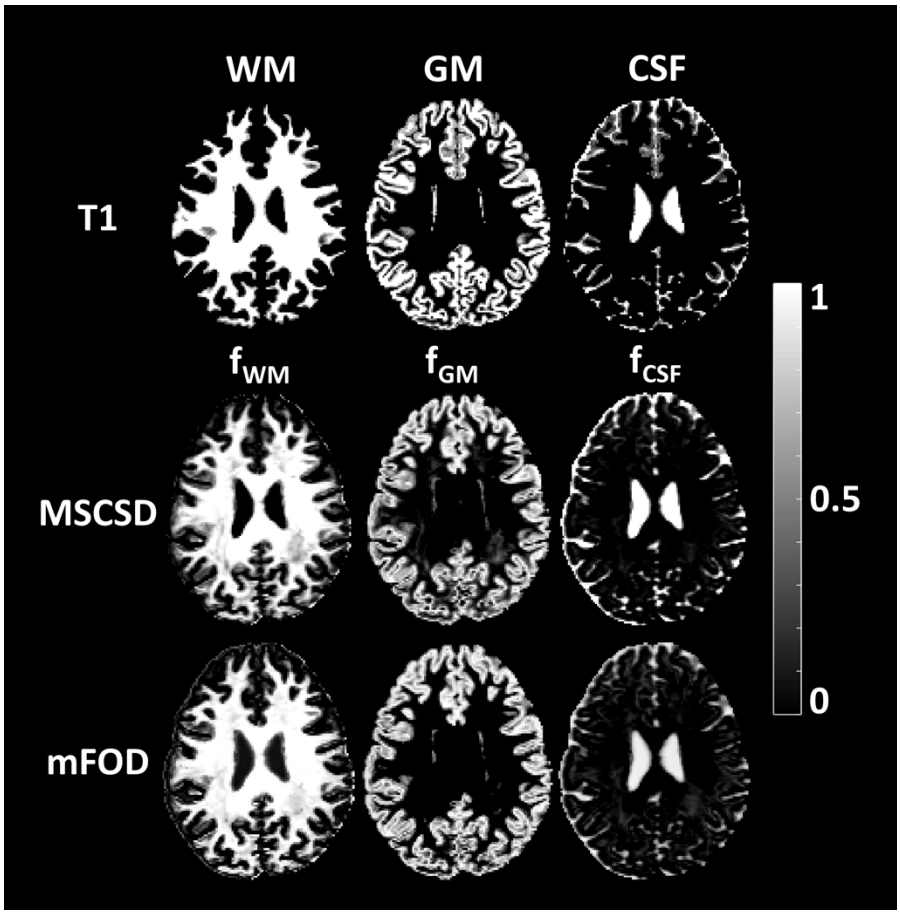

Figure 3: An example axial slice of the signal fractions estimated with MSCSD and mFOD in correspondence of different response functions as compared to the tissue segmentation obtained from the structural T1 image. Estimates with MSCSD and with mFOD are remarkably similar and have high anatomical correspondence with the tissue types that they are designed to represent.

FODs

The FODs estimated with MSCSD and mFOD in two cortical areas are shown in Fig. 4 and Fig. 5, for an example axial slice and an example coronal slice, respectively. The WM fiber orientation estimated with mFOD ($mFOD_1$) show remarkable similarity to the FOD estimated with MSCSD in WM. Both FODs have very sharp and comparable orientations in the vicinity of WM, but they tend to zero in deeper cortical GM. In contrast, the GM fiber orientation with mFOD ($mFOD_2$) show dominant and physiologically plausible peaks in most GM voxel, with orientation mostly perpendicular to that of the underlying WM. When $mFOD_1$ and $mFOD_2$ are linearly combined (mFOD-WS), a continuous vector field from WM to deep cortical GM is revealed.

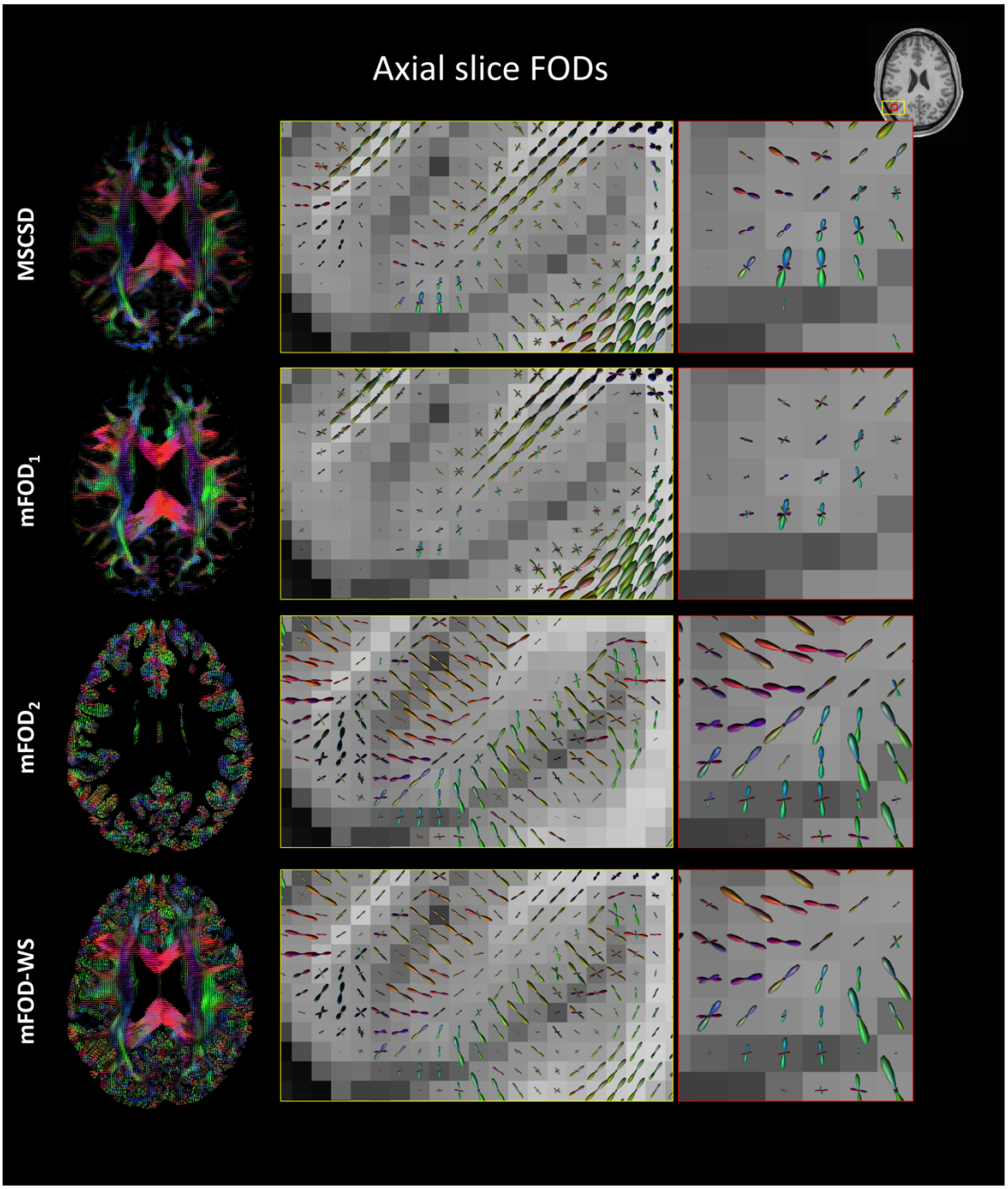

Figure 4: Fiber orientation distributions obtained with MSCSD and mFOD in an axial slice. The middle and the right columns show increasing zoom levels to highlight details of the cortical folding. $mFOD_1$ and $mFOD_2$ refer to the FODs computed when using response functions meant to represent WM and GM, respectively. mFOD-WS is the sum of $mFOD_1$ and $mFOD_2$ weighted by their corresponding signal fractions. $mFOD_2$ is non-zero only in GM and its proximity, and shows dominant orientations also in the deeper cortex, in contrast to both MSCSD and $mFOD_1$. mFOD-WS combines the information content of $mFOD_1$ in WM with that of $mFOD_2$ in GM.

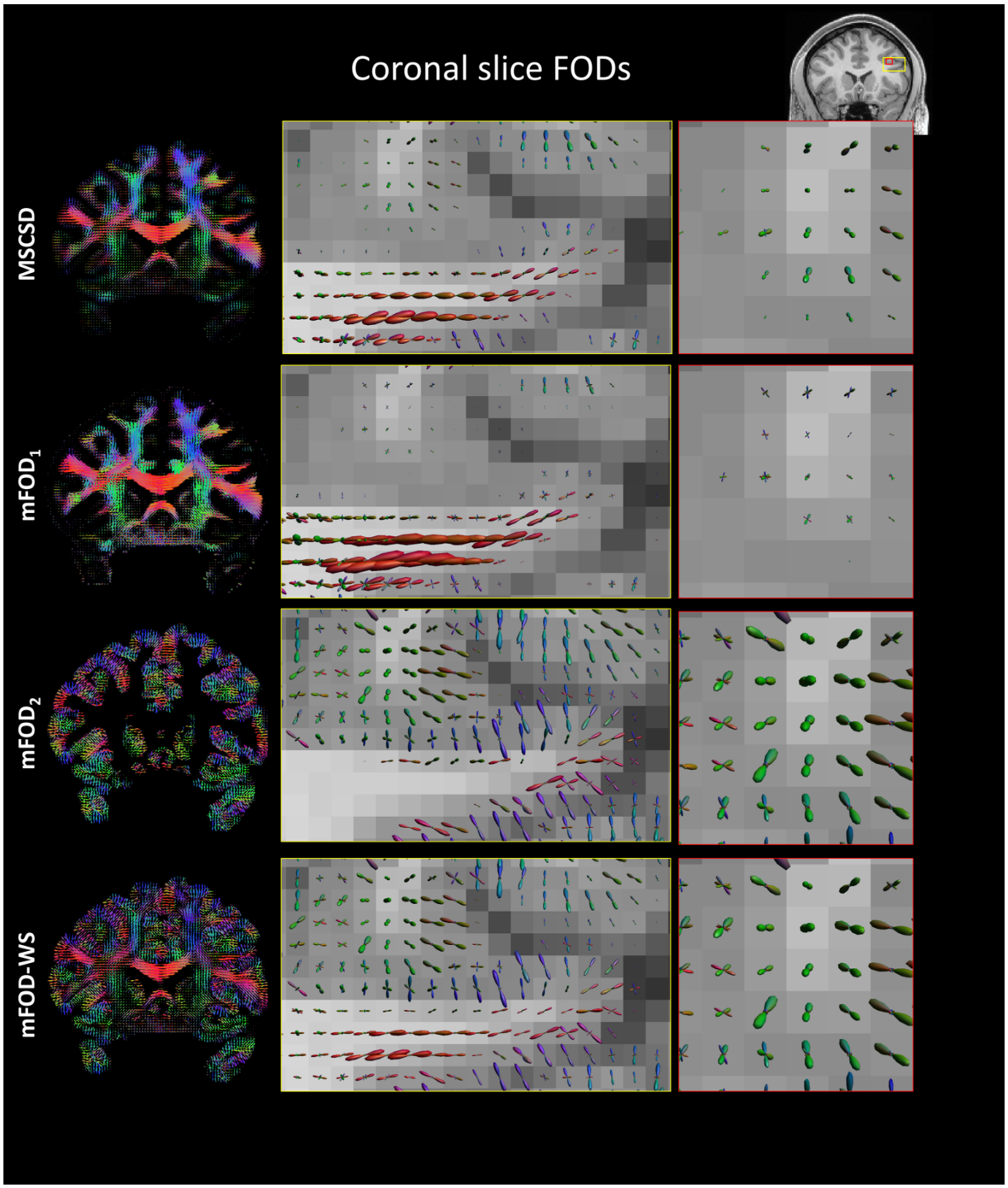

Figure 5: Fiber orientation distributions obtained with MSCSD and mFOD in a coronal slice. The middle and the right columns show increasing zoom levels to highlight details of the cortical folding. $mFOD_1$ and $mFOD_2$ refer to the FODs computed when using response functions meant to represent WM and GM, respectively. $mFOD_2$ is non-zero only in proximity of GM, and shows dominant orientations also in the deeper cortex, in contrast to both MSCSD and $mFOD_1$. $mFOD_1$ provides directional information in strong agreement with MSCSD but occasionally shows more peaks.

Fig. 6 shows an analysis of the peak orientations obtained with MSCSD and mFOD-WS as compared to the spatial direction normal to the cortical folding derived from the T1-weighted image with a structural tensor approach. When comparing the peak direction of MSCSD and mFOD-WS in WM, we observe that more than 70% of the WM voxels have an angular deviation smaller or equal than 10 degrees. In GM, the angular deviation between the two methods is larger, and mFOD-WS result in smaller angular deviation with the cortex normal than MSCSD.

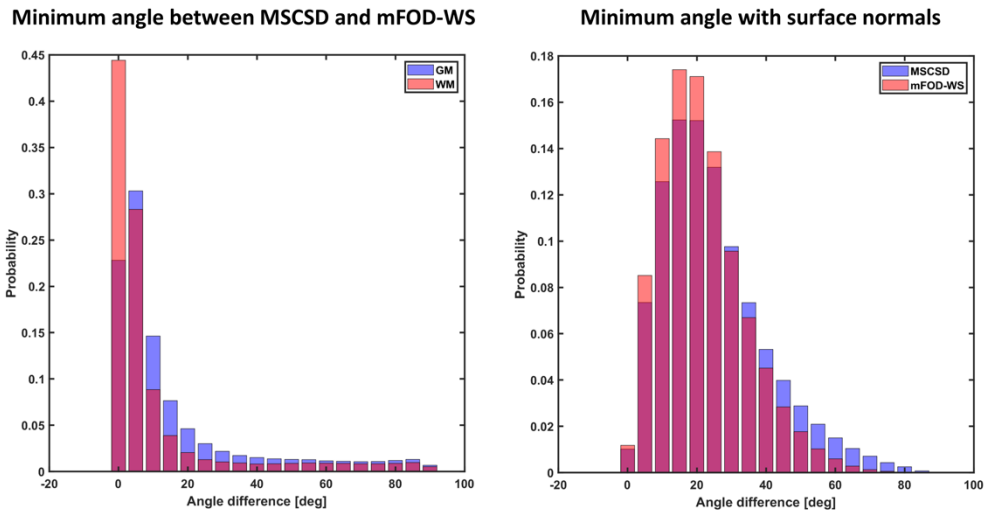

Figure 6: The left histogram shows the normalized frequency (probability) of the angle between the main orientation computed with MSCSD and mFOD-WS in GM and WM, respectively. The right histogram shows the probability of the angle difference between the normal direction to the GM/WM surface and main direction with MSCSD or mFOD-WS. With regards to the left plot, the two method have very small angle differences in WM, within 10 degrees in over 70% of voxels, whereas larger differences are observed in GM. When looking at the angle deviation as compared to the surface normal, the main direction computed in GM with mFOD-WS had remarkably lower deviation than that computed with MSCSD.

Fiber tractography

The results we obtained by performing deterministic fiber tractography on the FODs computed with MSCSD and mFOD-WS in a frontal lobe region are shown in Fig. 7. The tracts, which are color encoded according to the tissue type they are spatially traversing, are more densely reconstructed with mFOD-WS. Further, the tracts with mFOD-WS cover the GM more extensively and uniformly, and traverse the tissue with a more plausible shape to a deeper extent.

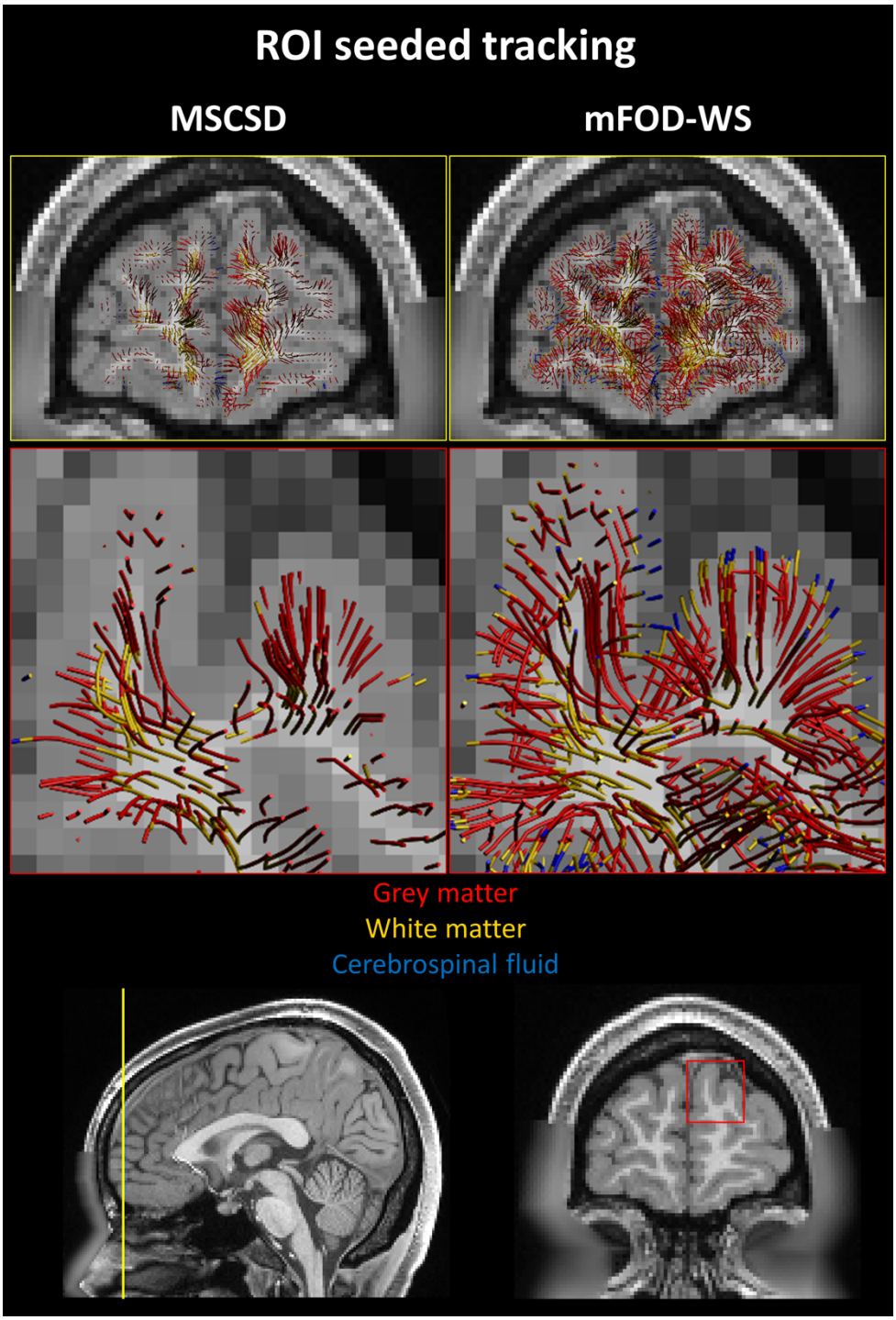

Figure 7: The fiber tracts obtained by tracking the FODs of MSCSD and mFOD-WS by seeding a frontal region (shown in yellow in the bottom left corner) with identical tracking parameters and FOD thresholds. The tracts are color encoded according to the tissue type they transverse, as determined on the structural T1 image. The tracking of mFOD-WS resulted in a more complete tracking of the frontal cortex as compared to MSCSD, with the tracts covering a larger distance within the cortex.

Subsequently, we performed whole brain fiber tractography of the FODs derived with MSCSD and mFOD, both individually ($mFOD_1$, $mFOD_2$) and after a weighted sum procedure (mFOD-WS). The tracking of $mFOD_1$ produces a whole brain reconstruction that is largely comparable to that of MSCSD, suggesting preservation of the WM tracking performances. The tracking of $mFOD_2$ results mostly in cortical reconstructions and short U-fibers, in-line with the tissue-specific nature of this FOD. The deterministic fiber tractography of mFOD-WS results in 694752 reconstructed tracts, 183821 more than those reconstructed with the FOD derived with MSCSD. After filtering out implausible tracts – i.e. tracts not starting or ending in GM, mFOD-WS reconstructed 594199 valid tracts, 130414 more than MSCSD. Among these, 42.1% have the first or the last tracked point in GM, as compared to 34.1% when performing tractography with MSCSD. This is qualitatively visible in the tissue-type encoded reconstruction of Fig. 8, which shows that mFOD-WS covers more extensively the GM as compared to MSCSD, although introducing some extra spurious fibers.

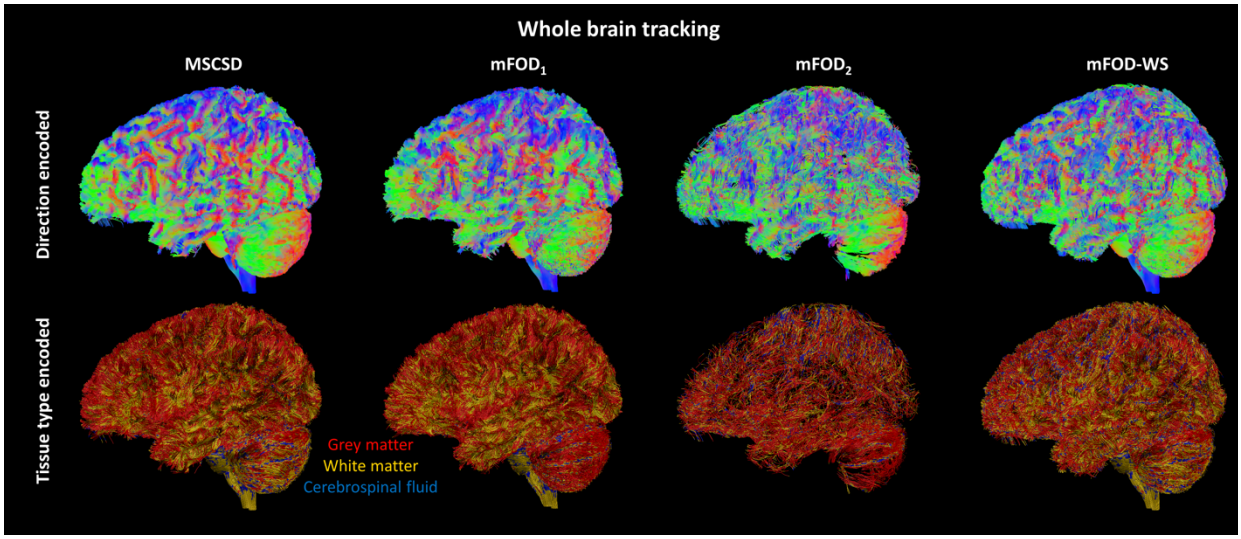

Figure 8 – Whole brain tracking of the FODs computed with MSCSD and with mFOD. The first row shows the tracts color encoded with the conventional color scheme, whereas the second row shows the same tracking color encoded by traversed tissue type (subsampled with factor 8). MSCSD and $mFOD_1$ provided similar tracking results, with the latter showing more spurious tracts outside the cortical folding, but also better characterization of the cerebellar cortex. The tracking of $mFOD_2$ resulted exclusively in cortical and short (U-fibers) connections. With mFOD-WS, a more complete coverage of the GM is achieved as compared to both $mFOD_1$ and MSCSD.

An example sagittal slab of the tracts reconstructed with MSCSD and mFOD-WS was obtained by cropping the whole brain fiber tractography, as shown in Fig. 9. In the first column, the tracts are color encoded according to their distance from the WM/GM interface (blue) to the GM/CSF interface (red). The results confirm that the tracts reconstructed with mFOD-WS consistently travel a longer distance within the cortical GM than with MSCSD, in-line with observations in Fig. 7. Further, the frontal, parietal and occipital side of the cortex appear to be better reconstructed with mFOD-WS.

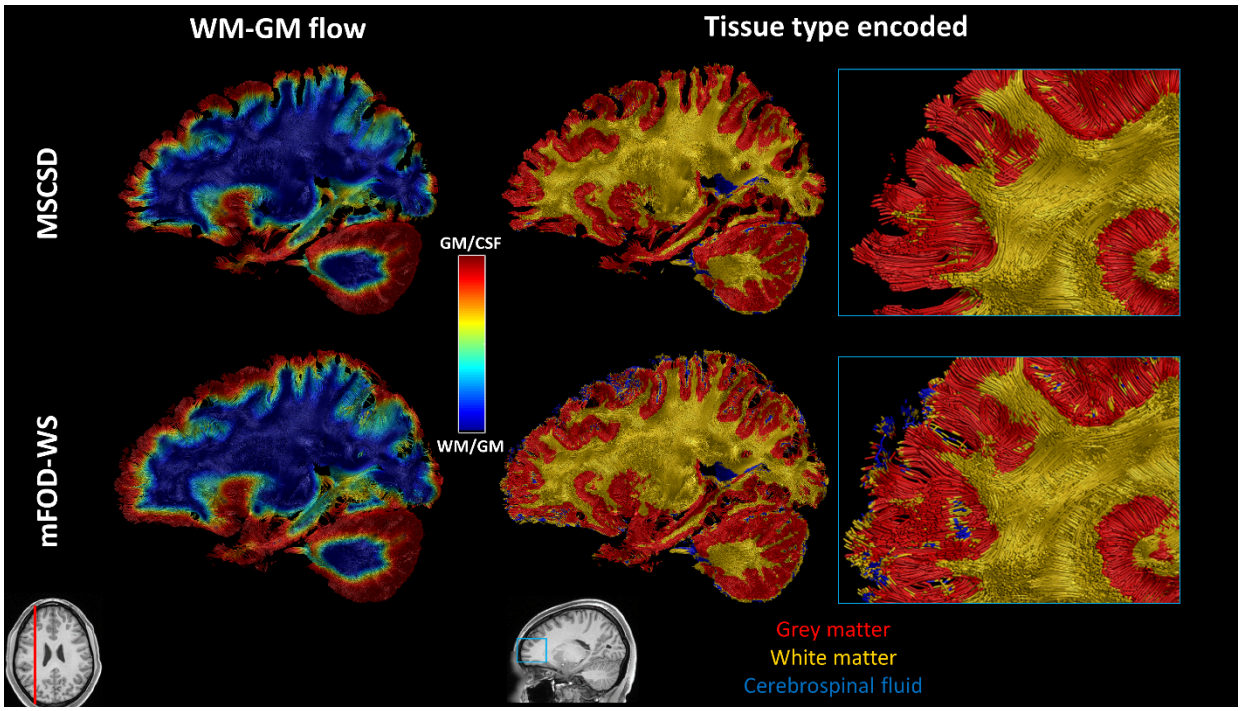

Figure 9 – A sagittal slab (red line in the bottom left picture) of the fiber tractographies obtained with the FODs from MSCSD and mFOD-WS. The first column shows the tracts color encoded according to their normalized distance from the GM/WM and the GM/CSF interfaces. The distance was determined in 3D as flow between the two surfaces using the same method we previously used to determine the cortex normal. The central and right column show the same sagittal slab color encoded by tissue type, and its zoom in a cortical region. The WM-GM flow color encoding shows that a deeper cortical tracking was achieved with mFOD-WS as compared to MSCSD, especially in the frontal and occipital areas. When looking at the tissue type encoded images, mFOD-WS resulted in a more complete and contiguous reconstruction of the cortical folding.

Discussion

In this work, we have introduced a framework to perform spherical deconvolution of multiple anisotropic response functions which allows to reconstruct multiple fiber orientation distributions (mFOD) for each voxel. With simulations and data from the Human Connectome Project, we have shown that i) it is possible to reconstruct two anisotropic FODs specific of WM and GM while also accounting for CSF partial volume, given sufficient SNR (greater or equal than 50 with respect to the b = 0 s/mm^2 data) is achieved. Further, we have shown that ii) mFOD improves the reconstruction of FODs in GM as compared to existing state-of-the-art methods, and that iii) this results in improved fiber tractography reconstruction in GM.

Feasibility of mFOD

The reconstruction of multiple anisotropic FODs is a hard numerical problem that requires the inversion of a matrix whose rank (number of measurements) is much lower than the number of possible solutions (FOD amplitudes on the unit sphere), a recurring challenge in deconvolution problems. Previous studies, as Tournier et al.[27] and Jeurissen et al.[23] used an L2 regularization term enforcing contiguity (smoothness) in the FOD amplitudes. In this work, we used a non-negative least-squares solver with L2 regularization encapsulated in an iterative solver. Taking into consideration that the mFOD formulation (eq. [2]) hosts multiple FODs, this might be suboptimal and introduce discontinuities in the solution. Nevertheless, our results suggest that mFOD does not propagate smoothness between multiple FODs, likely due to the attenuation of small perturbations operated by the median operator[29]. Indeed, the results of simulations, shown in Fig. 1 and Fig. 2, suggest that this approach allows to effectively disentangle the partial volume effects between mixtures of isotropic (n=1) and anisotropic (n=2) signal mixtures, if sufficient SNR is provided. In particular, the partial volume effects between WM and CSF are the easiest to disentangle, and an SNR equal or greater than 20 is sufficient to obtain accurate signal fractions separation and minimal angular error on the WM FODs. In contrast, the separation of GM from both WM and CSF is a harder task, probably as a result of the low anisotropy of this tissue type. Nevertheless, if an SNR equal or above 50 is achieved, mFOD can excellently preserve the ratios between different tissue types and estimate their mixtures with minimal biases (Fig. 2). While an SNR of about 50 might be difficult to achieve in clinical settings, accurate pre-processing and denoising[38], or even deep-learning based reconstructions[39] might mitigate this need. Furthermore, in both simulation I and simulation II the diffusion direction of GM was set perpendicular to that of WM, but in-vivo the two are likely to coincide as white matter bundles travel to their cortical endpoint perpendicularly[40], with exceptions such as the primary visual cortex[15] or the U-fibers adjacent to the cortex[41]. If the direction of the axons leaving the cortex (to the WM) wouldn't match that of intra-cortical axons, the results of simulations suggest that the GM FOD would be estimated with angular error between 10 (SNR 30) and 5 degrees (SNR 50), which are likely to perturbate the tracking trajectory. Furthermore, Fig. 3 shows that with in-vivo data the signal fraction map associated to GM is zero-valued in all non-GM voxels, and that it assumes a value of 1 in almost all GM voxels, which suggests excellent separation of the two tissues.

Why modelling GM?

The unique characteristic of mFOD is indeed the ability to reconstruct multiple FODs specific of the different employed signal models, as shown in Fig. 4 and Fig. 5. The figure shows that WM fiber orientations estimated with mFOD ($mFOD_1$) and MSCSD are very similar in GM, and that both rapidly assume a value of zero in GM with the default FOD thresholds. In contrast, the GM fiber orientations estimated with mFOD ($mFOD_2$) show consistent and well-defined diffusion directions for a large extent of the cortical GM. The performance improvement over MSCSD of mFOD in GM is explained by considering the improved tissue modelling in mFOD. Indeed, approaches as MSCSD essentially describes the WM and GM mixture as the sum of an anisotropic and an isotropic signal, similarly to the ball-and-stick approach[42], where the anisotropic signal is modelled with properties extracted from single fiber population WM[27,43,44]. In practice thus, by applying any constrained spherical deconvolution method in GM, one assumes the axonal component of GM to produce a similar signal to that of a WM bundle without crossing fibers. However, assuming cortical axons and dendrites to be identical to axons in the corpus callosum or part of the corticospinal tracts might be a stretch given their different diffusion signature[45]. Differently, in this work we represent the GM signal with a special case of the NODDI model[33], which represents a first

attempt to take into account additional effects as tortuosity[46] and intra to extra neurite signal ration into the deconvolution problem.

Multiple FODs: how do we use them?

One of the open challenges in the mFOD framework regards the choice of how to combine the multiple FODs computed by the method. In this work, we adopted a pragmatic approach and considered their weighted sum (mFOD-WS). This choice produced convincing and contiguous FODs, as shown in Fig. 4 and Fig. 5. However, this might be sub-optimal for fiber tracking approaches, as it might blur the peaks detected in the individual FODs. Future work is needed to establish whether dynamically tracking the locally larger FOD, or dynamically choosing the FODs most aligned to the tracking direction might represent better alternatives. Additionally, sparse solvers as those including L1 or L0 norm[47] could be taken into consideration to improve the FOD separation and minimize overfit. Nevertheless, when we compared the main peaks of mFOD-WS to those obtained with MSCSD (Fig. 6), we observed remarkable similarity between the two in WM, where an angle error smaller than 10 degrees was observed in over 70% of WM voxels. This suggests that mFOD-WS does not worsen the performances of spherical deconvolution in WM. In GM, mFOD-WS resulted in smaller angular deviations with respect to the cortex normal as compared to MSCSD. While the cortex normal might not be always representative of the direction with which axons are organized in the cortex, they represent an accepted assumption[14] and might serve as a comparison term between the two methods. Further, we observe that the average of the angular deviation between the cortex normal and mFOD-WS is 20 degrees, which is in-line with the angular error predicted in case of WM and GM mixtures at SNR 50 (Fig. 1).

Improved fiber tractography in GM

Fiber tractography is one of the main applications of spherical deconvolution techniques. When seeding deterministic tractography in a frontal region (Fig. 7), we obtained more tracts with mFOD-WS than with MSCSD with identical FOD thresholds. Further, the tracts reconstructed with mFOD-WS covered the cortical structure more extensively, and their geometrical configuration appeared more similar to previous reports of high resolution cortical dMRI[22]. Eventually, a similar tractography result might be achievable also with MSCSD by tuning the FOD threshold[48]. However, this is likely to introduce not only false positives in WM, but also to worsen the tracking in GM itself. Indeed, being the model used for GM not optimal, classic deconvolution methods are likely to produce a large number of spurious peaks[49]. When performing whole brain tractography, the use of mFOD-WS resulted in more tracts having a start or endpoint in the GM (+8%), and generally in more extensive GM coverage, as shown in Fig. 8. This was even more apparent when looking at a sagittal slab (Fig. 9), which showed how tracts could be followed in GM up to the GM/CSF interface, at the price of more spurious tracts as compared to MSCSD. Practically, this could have a major impact when performing fiber tractography from/to the cortex is critical as, for instance, pre-surgical planning[50] or structural connectivity studies[51]. Indeed, existing fiber tractography methods do not seed the tracking procedure in the cortex, but rather at the GM/WM interface or in the adjacent WM, potentially introducing a number of false positives[52]. For similar reasons, connectivity studies are often performed by first seeding WM or the WM/GM interface, then filtering the tracts with anatomical constraints [cit. ACT], and finally assigning the tracts to the closest GM node after spatial dilation, potentially introducing uncertainty in the assignment [cit.]. mFOD may contribute addressing these short comes, allowing to follow WM bundles with higher accuracy than existing methods from/to their cortical start/endpoint.

Limitations

To follow, we discuss some limitations of this work. The models used to describe WM and GM were arbitrarily chosen among popular methods, but their combination might not be the optimal representations to jointly estimate multiple FODs. The DKI model, here used in its simplified version with isotropic kurtosis[32], efficiently represents non-Gaussian signals with a limited number of parameters but is sub-optimal at accounting for direction dependent signal restrictions. Alternatively, geometric representations of the WM signal[53], as well as data driven methods[44] could also be explored. The choice of models here suggested for both WM (DKI) and GM (NODDI) is not meant to be final but is rather a proof of concept of the feasibility of mFOD with tissue specific models.

In Fig. 6, we used the cortex normal direction as a comparison for FODs computed with both MSCSD and mFOD. While it is reasonable to assume that the most axonal projects will traverse the cortex with a perpendicular trajectory, this is not always the case. Further, the method here employed to compute the normal trajectory is not accurate when the sulci are separated by less than 2 voxels and should therefore interpreted in sight of his limitations. The performances of mFOD have here been shown on a single subject but should be investigated on a larger cohort and with more clinically achievable protocols to generalize the observed results. Finally, while we have shown that mFOD improves the performances of spherical deconvolution and fiber tractography in GM, it remains to be proved to which extent such improvements will benefit clinical studies and structural connectivity investigations.

In conclusion, we have presented a framework (mFOD) to perform spherical deconvolution of multiple user chosen models, to simultaneously reconstruct multiple fiber orientation distributions. By accounting for WM and a GM specific models, we have shown that mFOD can improve the performances of spherical deconvolution in GM while retaining state-of-the-art methods in WM.

References

1. Einstein, A. Über die von der molekularkinetischen Theorie der Wärme geforderte Bewegung von in ruhenden Flüssigkeiten suspendierten Teilchen. *Ann. Phys.* **322**, 549–560 (1905).

2. Walter, J. A. & Hope, A. B. Proton magnetic resonance studies of water in slime mould plasmodia. *Aust. J. Biol. Sci.* **24**, 497–507 (1971).

3. Basser, P. J., Mattiello, J. & LeBihan, D. MR diffusion tensor spectroscopy and imaging. *Biophys. J.* **66**, 259–67 (1994).

4. Jones, D. K., Simmons, A., Williams, S. C. & Horsfield, M. A. Non-invasive assessment of axonal fiber connectivity in the human brain via diffusion tensor MRI. *Magn. Reson. Med.* **42**, 37–41 (1999).

5. Mori, S., Crain, B. J., Chacko, V. P. & van Zijl, P. C. Three-dimensional tracking of axonal projections in the brain by magnetic resonance imaging. *Ann. Neurol.* **45**, 265–9 (1999).

6. Mori, S., Wakana, S., van Zijl, P. C. M. & Nagae-Poetscher, L. M. *MRI Atlas of Human White Matter*. (Elsevier Science, 2005).

7. Tuch, D. S. *et al.* High angular resolution diffusion imaging reveals intravoxel white matter fiber heterogeneity. *Magn. Reson. Med.* **48**, 577–582 (2002).

8. Jeurissen, B., Leemans, A., Tournier, J.-D., Jones, D. K. & Sijbers, J. Investigating the prevalence of complex fiber configurations in white matter tissue with diffusion magnetic resonance imaging. *Hum. Brain Mapp.* **34**, 2747–66 (2013).

9. Schilling, K. *et al.* Can increased spatial resolution solve the crossing fiber problem for diffusion MRI? *NMR Biomed.* **30Schillin**, 1–16 (2017).

10. Xie, S. *et al.* How does B-value affect HARDI reconstruction using clinical diffusion MRI data? *PLoS One* **10**, 1–19 (2015).

11. Tournier, J.-D., Calamante, F., Gadian, D. G. & Connelly, A. Direct estimation of the fiber orientation density function from diffusion-weighted MRI data using spherical deconvolution. *Neuroimage* **23**, 1176–85 (2004).

12. Dell'acqua, F. *et al.* A Deconvolution Approach Based on Multi-Tensor Model to Solve Fiber Crossing in Diffusion-MRI. *Conf. Proc. IEEE Eng. Med. Biol. Soc.* **2**, 1415–8 (2005).

13. Hagmann, P. *et al.* Mapping the structural core of human cerebral cortex. *PLoS Biol.* **6**, 1479–1493 (2008).

14. Tozer, D. J. *et al.* Linking white matter tracts to associated cortical grey matter: A tract extension methodology. *Neuroimage* **59**, 3094–3102 (2012).

15. Kleinnijenhuis, M. *et al.* Layer-specific diffusion weighted imaging in human primary visual cortex invitro. *Cortex* **49**, 2569–2582 (2013).

16. McNab, J. A. *et al.* The Human Connectome Project and beyond: initial applications of 300 mT/m gradients. *Neuroimage* **80**, 234–45 (2013).

17. Feinberg, D. A. & Setsompop, K. Ultra-fast MRI of the human brain with simultaneous multi-slice imaging. *J. Magn. Reson.* **229**, 90–100 (2013).

18. Assaf, Y. Imaging laminar structures in the gray matter with diffusion MRI. *Neuroimage* 1–12 (2018). doi:10.1016/j.neuroimage.2017.12.096

19. Leuze, C. W. U. *et al.* Layer-specific intracortical connectivity revealed with diffusion MRI. *Cereb. Cortex* **24**, 328–339 (2014).

20. Aggarwal, M., Nauen, D. W., Troncoso, J. C. & Mori, S. Probing region-specific microstructure of human cortical areas using high angular and spatial resolution diffusion MRI. *Neuroimage* **105**, 198–207 (2015).

21. McNab, J. A. *et al.* Surface based analysis of diffusion orientation for identifying architectonic domains in the in vivo human cortex. *Neuroimage* **69**, 87–100 (2013).

22. Setsompop, K. *et al.* High-Resolution In Vivo Diffusion Imaging of the Human Brain With Generalized Slice Dithered Enhanced Resolution : Simultaneous Multislice (gSlider-SMS). **151**, 141–151 (2018).

23. Jeurissen, B., Tournier, J.-D., Dhollander, T., Connelly, A. & Sijbers, J. Multi-tissue constrained spherical deconvolution for improved analysis of multi-shell diffusion MRI data. *Neuroimage* (2014). doi:10.1016/j.neuroimage.2014.07.061

24. Dell'acqua, F. *et al.* A modified damped Richardson-Lucy algorithm to reduce isotropic

background effects in spherical deconvolution. *Neuroimage* **49**, 1446–58 (2010).

25. Pietsch, M. *et al.* A framework for multi-component analysis of diffusion MRI data over the neonatal period. *Neuroimage* **186**, 321–337 (2019).

26. Kamagata, K. *et al.* Connectome analysis with diffusion MRI in idiopathic Parkinson's disease: Evaluation using multi-shell, multi-tissue, constrained spherical deconvolution. *NeuroImage Clin.* **17**, 518–529 (2018).

27. Tournier, J. D., Calamante, F. & Connelly, A. Robust determination of the fibre orientation distribution in diffusion MRI: Non-negativity constrained super-resolved spherical deconvolution. *Neuroimage* **35**, 1459–1472 (2007).

28. Schilling, K. G. *et al.* Histologically derived fiber response functions for diffusion MRI vary across white matter fibers—An ex vivo validation study in the squirrel monkey brain. *NMR Biomed.* **32**, 1–17 (2019).

29. Guo, F., Leemans, A., Viergever, Max A, Dell'acqua, F. & De Luca, A. Damped Richardson-Lucy Deconvolution for Multi-Shell Diffusion MRI. in *International Society for Magnetic Resonance in Medicine2* (2018).

30. De Luca, A., Leemans, A., Bertoldo, A., Arrigoni, F. & Froeling, M. A robust deconvolution method to disentangle multiple water pools in diffusion MRI. *NMR Biomed.* 1–17 (2018). doi:10.1002/nbm.3965

31. Jensen, J. H., Helpern, J. a, Ramani, A., Lu, H. & Kaczynski, K. Diffusional kurtosis imaging: the quantification of non-gaussian water diffusion by means of magnetic resonance imaging. *Magn. Reson. Med.* **53**, 1432–40 (2005).

32. De Luca, A., Bertoldo, A. & Froeling, M. Effects of perfusion on DTI and DKI estimates in the skeletal muscle. *Magn. Reson. Med.* **78**, 233–246 (2017).

33. Zhang, H. G., Schneider, T., Wheeler-Kingshott, C. a & Alexander, D. C. NODDI: practical in vivo neurite orientation dispersion and density imaging of the human brain. *Neuroimage* **61**, 1000–16 (2012).

34. Kleinnijenhuis, M. *Imaging fibres in the brain*. (2014). doi:10.13140/2.1.4788.7689

35. Leemans, A., Jeurissen, B., Sijbers, J. & Jones, D. K. ExploreDTI: a graphical toolbox for processing, analyzing, and visualizing diffusion MR data. in *17th annual meeting of the International Society for Magnetic Resonance in Medicine, Honolulu, Hawaii, USA* 3537 (2009).

36. Kleinnijenhuis, M., Barth, M., Alexander, D. C., van Cappellen van Walsum, A. M. & Norris, D. G. Structure Tensor Informed Fiber Tractography (STIFT) by combining gradient echo MRI and diffusion weighted imaging. *Neuroimage* **59**, 3941–3954 (2012).

37. Pajevic, S. & Pierpaoli, C. Color schemes to represent the orientation of anisotropic tissues from diffusion tensor data: application to white matter fiber tract mapping in the human brain. *Magn. Reson. Med.* **42**, 526–40 (1999).

38. Veraart, J. *et al.* Denoising of diffusion MRI using random matrix theory. *Neuroimage* **142**, 394–406 (2016).

39. Koppers, S., Haarburger, C. & Merhof, D. Diffusion MRI Signal Augmentation: From Single Shell to

Multi Shell with Deep Learning. in 61–70 (2017). doi:10.1007/978-3-319-54130-3_5

40. Budde, M. D. & Annese, J. Quantification of anisotropy and fiber orientation in human brain histological sections. *Front. Integr. Neurosci.* **7**, 1–8 (2013).

41. Schilling, K. *et al.* Confirmation of a gyral bias in diffusion MRI fiber tractography. *Hum. Brain Mapp.* **39**, 1449–1466 (2018).

42. Tuch, D. S. Q-ball imaging. *Magn. Reson. Med.* **52**, 1358–72 (2004).

43. Dell'Acqua, F. *et al.* A model-based deconvolution approach to solve fiber crossing in diffusion-weighted MR imaging. *IEEE Trans. Biomed. Eng.* **54**, 462–72 (2007).

44. Tax, C. M. W., Jeurissen, B., Vos, S. B., Viergever, M. A. & Leemans, A. Recursive calibration of the fiber response function for spherical deconvolution of diffusion MRI data. *Neuroimage* **86**, 67–80 (2014).

45. Westin, C. F. *et al.* Q-space trajectory imaging for multidimensional diffusion MRI of the human brain. *Neuroimage* **135**, 345–362 (2016).

46. Sen, P. N. & Basser, P. J. A model for diffusion in white matter in the brain. *Biophys. J.* **89**, 2927–2938 (2005).

47. Daducci, A., Van De Ville, D., Thiran, J. P. & Wiaux, Y. Sparse regularization for fiber ODF reconstruction: From the suboptimality of$\ell 2$and$\ell 1$priors to$\ell 0$. *Med. Image Anal.* **18**, 820–833 (2014).

48. Aerts, H., Dhollander, T. & Marinazzo, D. Evaluating the performance of 3-tissue constrained spherical deconvolution pipelines for within-tumor tractography. *bioRxiv* (2019).

49. Parker, G. D. *et al.* A pitfall in the reconstruction of fibre ODFs using spherical deconvolution of diffusion MRI data. *Neuroimage* **65**, 433–448 (2013).

50. Mormina, E. *et al.* Optic radiations evaluation in patients affected by high-grade gliomas: a side-by-side constrained spherical deconvolution and diffusion tensor imaging study. *Neuroradiology* **58**, 1067–1075 (2016).

51. Beare, R. *et al.* Altered structural connectivity in ADHD: a network based analysis. *Brain Imaging Behav.* **11**, 846–858 (2017).

52. Maier-Hein, K. H. *et al.* The challenge of mapping the human connectome based on diffusion tractography. *Nat. Commun.* **8**, (2017).

53. Ferizi, U. *et al.* A ranking of diffusion MRI compartment models with in vivo human brain data. *Magn. Reson. Med.* **72**, 1785–1792 (2014).